metals

MDPI

Article

Optimizing Wear Resistance and Tensile Strength of Nickel-Based Coatings through Tungsten Carbide Reinforcement

Li Zhang [1,2], Shengli Li [1,*], Chunlin Zhang [1], Shihan Zhang [3], Xingang Ai [1] and Zhiwen Xie [3,*]

[1] College of Materials and Metallurgy, University of Science and Technology Liaoning, Anshan 114051, China; zhangli_198803@126.com (L.Z.); zhangchunlin@email.cn (C.Z.); aixingang@ustl.edu.cn (X.A.)
[2] College of Materials Science and Engineering, Yingkou Institute of Technology, Yingkou 115004, China
[3] College of Mechanical Engineering and Automation, University of Science and Technology Liaoning, Anshan 114051, China
* Correspondence: lishengliustledu@163.com (S.L.); xzwustl@126.com (Z.X.)

Abstract: While the addition of WC increases the hardness and wear resistance of coatings, an excessive WC content can also induce crack initiation and propagation, increasing brittleness and leading to premature failure. Therefore, in this study, WC particles were incorporated into nickel-based coatings by plasma-arc surfacing to optimize their content and distribution, balancing their tensile properties and wear resistance. The coatings were comprehensively evaluated through microstructural analysis, hardness testing, wear resistance assessment, and tensile testing. The results show that as the mass fraction of WC increased from 45% to 65%, the increase in carbon significantly promoted the formation of M_7C_3, M_6C, and $M_{23}C_6$ carbides and suppressed the formation of the γ-phase. The microstructural analysis showed that the content of massive carbides increased significantly with the increasing WC content, and the XPS analysis further confirmed that the changes in the WC and Cr_7C_3 phases were particularly pronounced in the high-WC coating. The 65% WC coating showed higher hardness (a 232 increase in $HV_{1.0}$), a lower and more stable coefficient of friction (0.42), and better wear resistance than the 45% WC coating, with a wear rate of 3.329×10^{-6} $mm^3/(N{\cdot}m)^{-1}$, which was 3.709×10^{-6} $mm^3/(N{\cdot}m)^{-1}$ lower than that of the 45% WC coating. The conventional tensile test results show that the maximum stress and strain of the 45% WC coating were 71% and 36% higher than those of the 65% WC coating, respectively. In addition, the 45% WC coating exhibited better ductility and quasi-cleavage characteristics, whereas the 65% WC coating showed typical brittle cracking behavior. The results of the field tensile tests also showed that the fracture time of the 65% WC coating was 27 s shorter than that of the 45% WC coating. Overall, the 45% WC coating had a good combination of strength and toughness.

Keywords: plasma-arc surfacing; WC particles; wear resistance; tensile properties

check for updates

Citation: Zhang, L.; Li, S.; Zhang, C.; Zhang, S.; Ai, X.; Xie, Z. Optimizing Wear Resistance and Tensile Strength of Nickel-Based Coatings through Tungsten Carbide Reinforcement. *Metals* **2024**, *14*, 1097. https://doi.org/10.3390/met14101097

Academic Editor: Pierpaolo Carlone

Received: 12 August 2024
Revised: 18 September 2024
Accepted: 22 September 2024
Published: 24 September 2024

Copyright: © 2024 by the authors. Licensee MDPI, Basel, Switzerland. This article is an open access article distributed under the terms and conditions of the Creative Commons Attribution (CC BY) license (https://creativecommons.org/licenses/by/4.0/).

1. Introduction

As critical components of the hot-rolling line, both rolls and descaling rolls endure severe surface degradation, shortened service life, and diminished reliability due to prolonged exposure to high temperatures, heavy loads, and abrasive environments. The reduced service life and accelerated wear of these components have critically hindered the high-quality development of the industry. To address these challenges, surface-engineering technology has emerged as a pivotal driver for the evolution of the metallurgical industry [1,2].

Nickel-based alloys are widely used in the metallurgical, aerospace, and petrochemical industries due to their superior corrosion resistance, self-lubricating properties, and exceptional high-temperature oxidation stability [3]. However, the use of nickel-based alloys in high-temperature, high-stress environments is often limited by their suboptimal wear resistance and tensile strength, making a single material inadequate for practical applications [4]. Consequently, researchers have begun to improve the performance of nickel-based alloy

coatings by introducing strengthening phases. Among these, WC stands out as a ceramic material with high hardness, a high melting point, and exceptional corrosion resistance, making it a popular choice in various composite coatings [5,6].

Numerous studies have shown that the incorporation of WC particles results in significant improvements in the hardness and wear resistance of coatings. For example, increasing the WC content from 5% to 10% resulted in a significant improvement in both hardness and wear resistance, with a 10% WC content providing optimum wear resistance [7]. When the WC content was further increased to 20%, the coating showed superior wear resistance and achieved the lowest wear rate [8–11]. When the WC content was increased from 5% to 30%, the hardness increased significantly and continued to increase at 35%. However, at this point, the microhardness began to show fluctuations with the increasing content [12,13]. Li et al. [14] reported that at a 40% WC content, the hardness of coatings reached 474.8 HV, while the coefficient of friction was minimized. This was attributed to the solid solution strengthening of the WC particles and the grain refinement effect. Further investigations showed that both the wear resistance and hardness were optimized within the WC content range of 40–50% [15,16]. Overall, the hardness and wear resistance of the coatings showed a consistent improvement when the WC content remained below 50%.

However, although increasing the WC content enhances the hardness and wear resistance of coatings, it is also accompanied by a significant rise in brittleness, which induces cracks and, ultimately, compromises overall performance. For example, when the WC content was elevated from 10% to 30%, both the hardness and wear resistance improved substantially, particularly within the 20–30% range, where the performance peaked. However, once the WC content exceeded 30%, the brittleness of the coating increased significantly, leading to crack formation and a plateau in performance [17]. Similar phenomena have been observed in other studies. When the WC content reached 30 wt.%, the hardness and microstructural homogeneity of the coating attained a high level, but beyond this point, some WC particles dissolved and formed brittle phases, resulting in crack initiation and reduced coating performance [18–20]. For coatings with high WC contents, it was shown that the hardness and wear resistance of the coatings increased steadily as the WC content was increased from 5% to 50%, and the best was achieved at 40–45 wt.%. However, when the WC content exceeded 45%, cracks began to form, resulting in a deterioration of the mechanical properties [21,22]. In particular, when the WC content exceeded 50%, the increased brittleness led to cracking, which had a negative effect on the wear resistance despite further increases in hardness [23,24]. The occurrence of cracks often leads to premature coating failure, which underscores the need for in-depth studies of the tensile properties of these coatings. Current studies on the tensile properties of coatings are relatively limited and have mostly focused on coatings with low WC contents. For example, Huang et al. [16] found that the tensile strength and ductility of coatings were optimal at a WC content of 2%, but as the WC content increased, the coatings exhibited increased brittleness, leading to the formation of fatigue cracks and oxidized wear. In addition, the studies by He et al. [25] and Bao et al. [26] showed that under optimum process conditions, coatings with WC contents of 15–17% could achieve a maximum tensile strength of 242 MPa.

In summary, minimizing cracking while maintaining excellent tensile properties and improving the hardness and wear resistance of WC coatings remains a key challenge in the current research. To address this issue, two high-WC coatings, 45% WC and 65% WC, were selected in this study to investigate the optimum distribution of WC particles. The aim was to achieve a balance between abrasion resistance and tensile properties, thereby improving the overall performance and extending the life of the coatings.

2. Materials and Methods

Utilizing plasma-arc surfacing, nickel-based WC coatings were successfully applied to a 42CrMo roll surface. The comprehensive results of the chemical composition analysis for the substrate are presented in Table 1.

Table 1. Chemical composition of 42CrMo substrate (wt.%).

C	Mn	Si	Cr	Mo	P	S	Fe
0.39	0.56	0.19	0.11	0.15	≤0.015	≤0.015	Base

The coatings were composed of a transition layer and a hard surface layer, the latter characterized by its exceptional hardness. The hard surface layer was predominantly reinforced with spherical tungsten carbide particles, which were bonded with the nickel-based alloy Ni45. In contrast, the transition layer was composed solely of Ni45 powder. The chemical compositions of the nickel matrix composites with WC mass fractions of 45% (S1) and 65% (S2), along with detailed information regarding the transition layer, are presented in Table 2. Figure 1a,b illustrate the powder morphology and particle size distribution of the coatings for S1 and S2, respectively. As shown in the figures, both powders exhibited smooth, defect-free, spherical surfaces with an average particle size of approximately 70 µm.

Table 2. Chemical compositions of powders (wt.%).

Label	W	C	Si	Cr	Fe	B	Ni
45% WC	43.14	2.16	2.22	8.44	1.84	1.67	Bal
65% WC	62.32	2.8	1.42	5.37	1.23	1.06	Bal

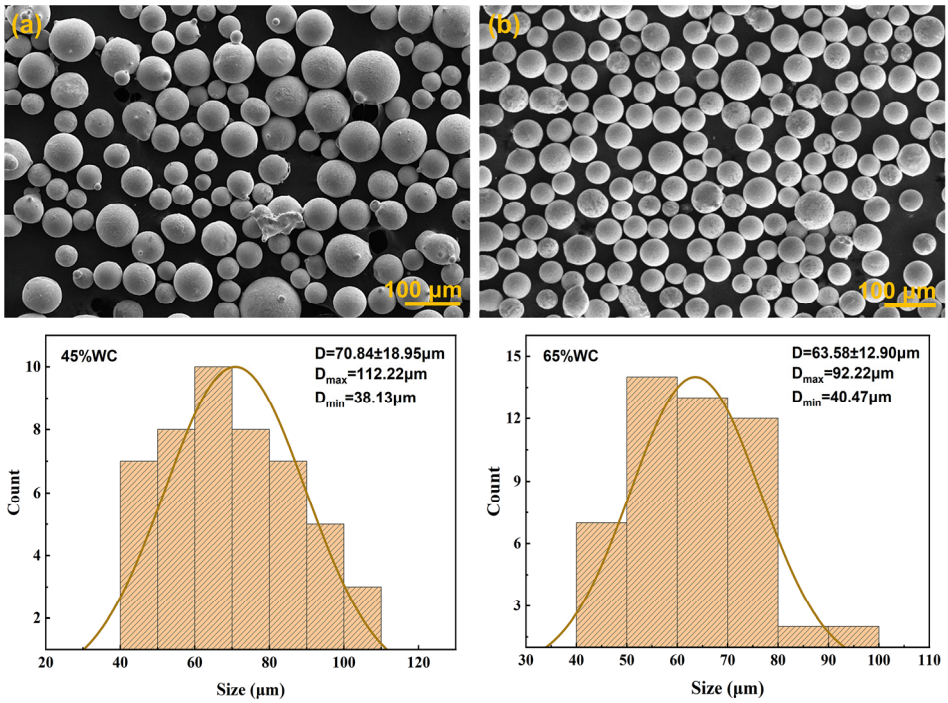


Figure 1. SEM images and particle sizes: (**a**) S1; (**b**) S2.

The DML-V03BD (Shanghai Duomu Industrial Co., Ltd., Shanghai, China) plasma-arc surfacing equipment was employed to apply coatings onto the surfaces of 42CrMo rolls. The specific operational parameters were configured as follows: a plasma current of 130 A, maintaining a consistent scanning speed of 120 mm/min, adjusting the rate of ionized gas flow to 3 L/min, controlling the powder feeding speed at 44 g/min, adjusting the powder gas flow rate to approximately 5 L/min, and finally sustaining a protective gas flow rate of 13 L/min. Prior to commencing plasma-arc surfacing, the 42CrMo rolls underwent meticulous grinding and preheating to 550 °C. This preheating phase was essential for reducing thermal gradients during the surfacing process, thereby minimizing induced stresses and preventing defects such as distortion and cracking. Moreover, preheating

markedly enhanced the adhesion of the subsequent coatings. The entire preparation process took place within a specially designed furnace and gradually cooled until it reached room temperature. The microstructures of the coatings were analyzed using aqua regia solution. The microstructural and fracture morphology of the samples was examined using a Carl Zeiss Sigma 500 scanning electron microscope (Jena, Germany). The elemental compositions were analyzed using a combined Bruker X' Flash and energy-dispersive X-ray spectroscopy (EDX) analyzer (Billerica, MA, USA). In order to conduct a thorough assessment of the phase compositions of the coatings, a Bruker D8 Advance X-ray diffractometer (Bruker, Karlsruhe, Germany) measured the diffraction angle within the range of 20° to 100°. X-ray photoelectron spectroscopy (XPS) spectra were carefully recorded using a Thermo Scientific K-Alpha spectrometer equipped (Waltham, MA, USA) with a monochromatic Al Kα X-ray source (with a spot size of 450 μm and a filament current of 6 mA). The survey XPS spectrum scan was performed at 150 eV with a step size of 1 eV, while the high-resolution XPS spectrum scan was performed at 50 eV with a finer step size of 0.1 eV. To ensure the accuracy of the binding energy measurements, all spectral data were carefully calibrated using the surface-contaminated C 1 s peak at 284.8 eV as a reference. Microhardness measurements were performed on sample cross-sections using an HV-1000 microhardness tester (Shanghai Materials Tester Machine Co., Shanghai, China) at intervals of 0.2 mm. The experimental load was 9.8 Newtons (equivalent to 1000 g; HV 1.0), and the loading time was 10 s. The hardness values were measured on three lines on the surface of each cross-sectional sample to determine the hardness at each point, and the average value was calculated. The tensile tests in this study were carried out using two different machines. Conventional tensile tests were performed with an ETM105D universal testing machine (Shenzhen Wance Testing Machine Co., Ltd., Shenzhen, China). The specimen thickness was 3 mm, with the exact dimensions and specimen directions shown in Figure 2a,b. To capture the microstructural evolution during strain, in situ tensile experiments were performed with a scanning electron microscope (SEM) equipped with a Kammrath & Weiss loading stage (Schwerte, Germany). The strain rate was precisely set to 1 μm/s, with a thickness of 1 mm, as shown in Figure 2a,c. In addition, the wear resistance of the S1 and S2 coatings was systematically evaluated using an MFT-5000 tribometer (Rtec Instruments, San Jose, CA, USA). Considering the operating conditions of the descaling rolls, GCr15 steel balls with a diameter of 9.525 mm were selected as the wear-resistant material, with an experimental load of 15 N, a frequency of 17 Hz, and a wear mark length of 6 mm. The 3D wear morphologies were acquired utilizing a white light interferometer (ZYGO Corporation, Middlefield, CT, USA). The specific specimen dimensions and sampling direction are shown in Figure 2a,c. The wear and tensile data represent the average of three replicates performed at room temperature.

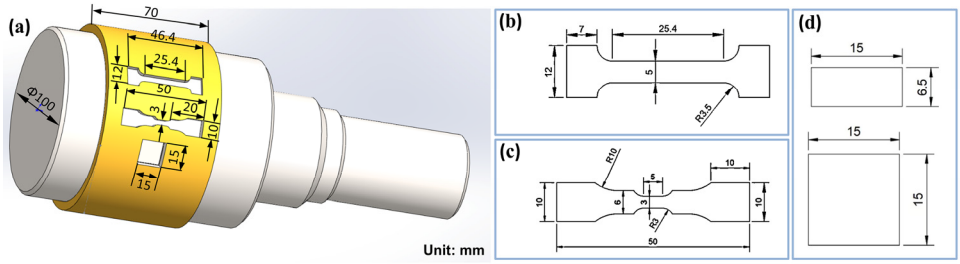


Figure 2. Sample size: (**a**) roll diagram; (**b**) tensile specimen size; (**c**) in situ tensile sample size; and (**d**) friction wear sample size.

3. Results and Discussion

3.1. Microstructures of the Coatings

Figure 3a,b show the microstructures of the S1 and S2 alloy coatings, respectively. The final coating thicknesses, averaged over 10 measurements, were found to be 5.74 mm for S1 and 5.19 mm for S2. These thicknesses exceeded the current standards for high-WC hard-

phase coatings. Figure 3(a2) shows that the S1 coating had a thin interlayer surrounding the WC particles, indicating metallurgical interactions between the WC particles and the matrix. The increased solubility of WC in the S2 coating resulted in a wider metallurgical interface, as shown in Figure 3(b2). Figure 3(b1) shows that the higher concentration of WC precipitation increased the proportion of carbon elements, which promoted carbide formation in the microstructure. As a result, W atoms tended to combine with Cr to form complex carbides with lower melting points (e.g., M_6C, M_7C_3, and $M_{23}C_6$), thereby altering the surface microstructure. In addition, Table 3 shows that the nickel-based zone F of the S2 coating had a carbon concentration of 19.78%, which was a significant increase of 9.71% compared with zone C in the S1 coating. This suggests that the increased WC particles in the S2 coating increased the likelihood of thermal decomposition, resulting in higher carbon release. The high WC content reduced the inter-atomic distance, thereby promoting atomic diffusion. As a result, the metallurgical bonding interface expanded [27,28]. The chemical compositions of regions A, B, D, and E in Figure 3(a3,b3) are detailed in Table 3. The grey phases in regions A and D were mainly composed of various forms of W_2C, while the eutectic in region B was mainly composed of the γ-phase. The bright white region E consisted mainly of M_7C_3 carbide. The carbide concentration on the surface of the S2 coating was significantly higher than that of the S1 coating. This can be attributed to the fact that at elevated temperatures, a higher concentration of WC particles enhances the diffusion interactions between carbon and tungsten, thereby facilitating the formation of complex carbide structures [29].

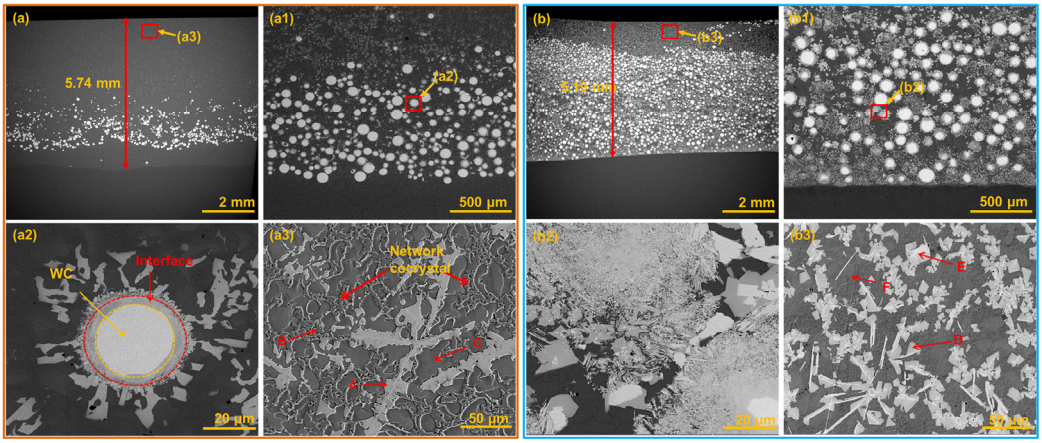


Figure 3. Cross-sectional SEM images of the coatings: (**a**) S1 coating; (**b**) S2 coating; (**a1**) Bottom of the S1 coating; (**a2**) WC particles in the red box of (**a1**); (**a3**) Top of the S1 coating in the red box of (**a**); (**b1**) Bottom of the S2 coating; (**b2**) WC particles in the red box of (**b1**); (**b3**) Top of the S2 coating in the red box of (**b**).

Table 3. Chemical composition of each designated area (at. %).

Area	W	Cr	C	Fe	Ni
A	35.85	15.79	17.85	5.20	25.31
B	0.57	4.45	9.63	50.38	34.97
C	-	4.74	9.97	22.53	62.76
D	49.02	14.64	10.02	4.09	20.23
E	43.52	10.84	20.32	8.98	16.34
F	-	6.60	19.78	10.00	63.62

3.2. Phases of the Coatings

Figure 4 shows the XRD patterns of the S1 and S2 coatings. In the S1 coating with a 45% WC content, fewer diffraction peaks were observed, but the peak intensities of the γ-phase were significantly higher at 44.05° and 51.16°, indicating the strong stability of the γ-phase within the crystal structure. This stability is critical for improving the mechanical

properties and durability of coatings, as the presence of the γ-phase is typically associated with improved toughness and fatigue resistance [30,31]. In contrast, the peak intensity of the γ-phase in the S2 coating with a 65% WC content was significantly reduced, indicating that the formation of the γ-phase was inhibited with the increase in the WC content, while more carbide phases (e.g., M_7C_3, M_6C, and $M_{23}C_6$) were generated, appearing at the diffraction angles of 35.57°, 43.11°, and 48.17°, respectively [32]. The formation of carbides increased the hardness of the coating to some extent, particularly due to the cubic crystal structure of these carbides (e.g., M_7C_3 and $M_{23}C_6$), which imparted significant hardness and wear resistance to the material [33,34]. However, excessive carbide formation also increases the brittleness of coatings, making them more susceptible to cracking. Ma et al. [35] demonstrated that an increase in the carbide phase typically results in a greater susceptibility to crack initiation in coatings with higher WC contents.

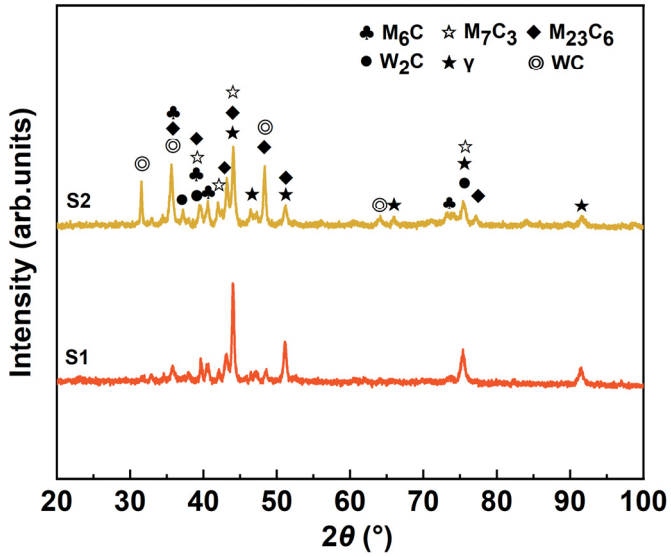


Figure 4. XRD patterns of S1 and S2.

In addition, the peak intensity of the undecomposed WC phase was higher in the S2 coating, indicating a greater presence of undecomposed WC particles within the coating. This can be attributed to the high melting point of WC, which is 2785 °C, significantly higher than the 900–1400 °C melting range of nickel-based alloys. As a result, WC particles are less likely to fully decompose during the metallurgical process. As the WC content increases, the particle spacing decreases, promoting an ordered arrangement of WC particles, which, in turn, increases the crystallinity of the coating, improving both its hardness and wear resistance [36,37]. However, Kaçmaz et al. [38] pointed out that while undecomposed WC particles can improve hardness, an excessive amount of WC particles can increase the brittleness of the coating, thereby reducing its toughness and impact resistance.

3.3. XPS Analyses of the Coatings

The chemical state evolution of the elements in the S1 and S2 coatings was carefully studied via X-ray photoelectron spectroscopy. The grey line in Figure 5 represents the raw data, while the black line corresponds to the fitted data. Figure 5a displays the survey spectra, revealing the presence of Cr, Fe, Ni, W, C, and O in the coatings. Notably, the Ni 2p and Fe 2p spectral intensities were significantly higher in the S1 coating, indicating an enrichment of Ni and Fe on the surface. The O 1s spectral line likely arose from minor surface oxidation during cooling, air exposure, or post-deposition processing. In the Fe 2p spectral line, three distinct binding energy states were identified in both the S1 and S2 coatings. These were identified as Fe-C bonds, corroborated by the literature [39,40], and further supported by the presence of the C-Fe bond in the C 1s spectral line in Figure 5f [41]. The Cr 2p spectral line exhibited spin–orbit coupling, resulting in two peaks corresponding

to Cr $2p_{3/2}$ and Cr $2p_{1/2}$. These peaks were observed within the ranges of 574.3–583.9 eV and 577.0–587.1 eV, respectively, reflecting the characteristic energy separation between the two spin–orbit components [42,43]. In the S2 coating, the Cr-C binding energy was measured at 574.5 eV, which was 0.2 eV higher than that of the S1 coating, by 0.2 eV. The binding energy of 283.0 eV observed in the C 1s spectral line corresponded to Cr_7C_3-type carbide [39], indicating that Cr existed in a partially stabilized Cr_7C_3 phase within the S2 coating. The observed increase in the binding energy suggested significant alterations in the chemical environment of the Fe and Cr atoms as the WC content increased. The interaction between Fe, Cr, and WC likely led to a reduction in the electron density, thus increasing the binding energy [42]. In the Ni 2p spectral line (Figure 5e), the satellite peak at 879.0 eV in the S2 coating was 0.6 eV lower compared with that of the S1 coating. Figure 5f illustrates that the W 4f peaks in the S1 coating were at 31.8 eV and 33.8 eV, closely corresponding to the W 4f energy level of WC [44,45]. Conversely, in the S2 coating, the W-C bond binding energy increased by 0.2–0.3 eV, signifying that the Ni 2p and W 4f peaks shifted negatively and positively, respectively, as the WC content rose. This phenomenon implies that charge transfer from the WC to Ni occurred in the S2 coating, resulting in opposite shifts in the nuclear energy levels of Ni and WC [46]. The C 1s spectra in Figure 5f show that the C-W bond in the S2 coating was at 283.8 eV [45], representing an increase of 0.3 eV relative to the S1 coating. This increase indicated that the higher WC content strengthened the W-C bond, suggesting more pronounced interactions between tungsten and carbon atoms, thereby further elevating the binding energy of the C-W bond.

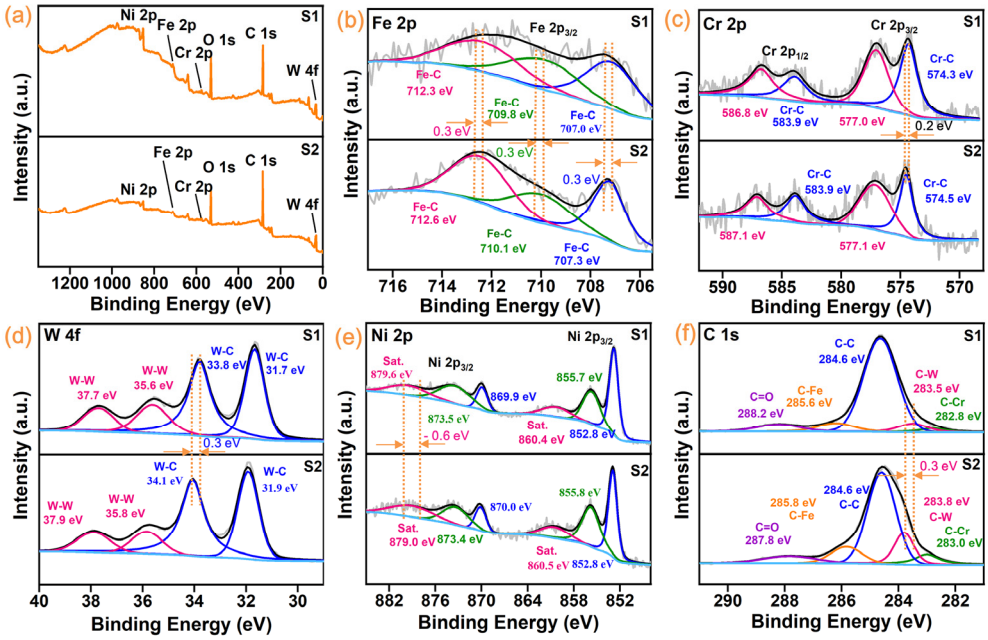


Figure 5. XPS spectra of S1 and S2 coatings: (**a**) survey spectra; (**b**) Fe 2p spectra; (**c**) Cr2p spectra; (**d**) W4f spectra; (**e**) Ni2p spectra; and (**f**) C1 s spectra.

3.4. Hardness of the Coatings

Figure 6a,b show the hardness measurements in different regions of the coatings, highlighting significant differences between the S1 and S2 coatings. Specifically, the blue boxes in Figure 6a show the average hardness values, with S1 exhibiting a hardness of 506 $HV_{1.0}$, while S2 reached 738 $HV_{1.0}$. Figure 6b further shows that the hardness of the S2 coating was significantly higher than that of S1 in the areas of WC particles, particle edges, and the nickel alloy substrate. These results are consistent with the existing literature on WC-reinforced coatings, which has consistently shown that the inclusion of WC significantly increases the hardness of coatings [47–50]. In the S2 coating, the WC secondary phase was uniformly distributed, which not only enhanced the strengthening effect of the matrix

but also improved the hardness by hindering dislocation movement. The large-scale dissolution of WC particles allowed the C and W elements to enter the matrix and form a solid solution, which, in turn, induced lattice distortion that increased the stress required for dislocation slippage, in accordance with the classical theory of solid solution strengthening. This theory states that lattice strain induced by solute atoms increases the strength and hardness of a material [51]. In addition to solid solution strengthening, the hardness and strength of the S2 coating also benefited from particle strengthening. WC particles were uniformly distributed throughout the matrix, creating a composite strengthening effect. The synergistic interaction between these mechanisms significantly increased the hardness and strength of the coating while improving its thermal stability [52]. The XRD data and microstructural analysis show that the S2 coating contained a significant amount of Cr_7C_3 and W_2C phases, which not only contributed to the overall strength and hardness of the coating but also improved its wear resistance.

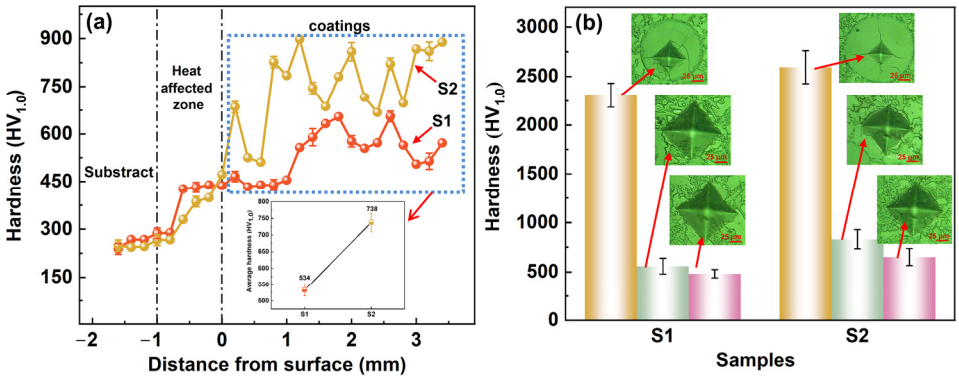


Figure 6. (**a**) Cross-sectional hardness distribution of the coatings; (**b**) surface hardness of distinct phases in the coatings.

3.5. Wear Resistance of the Coatings

3.5.1. Wear Behavior and 3D Morphological Analysis

The friction coefficient curves in Figure 7a show that the S1 coating initially exhibited a low friction coefficient during the early stages of sliding. However, as the sliding time progressed, particularly after the 3 min mark, the friction coefficient of S1 rapidly escalated to 0.52 and then stabilized. This sharp escalation in the friction coefficient was primarily attributed to the increase in the surface temperature during sliding, which led to the softening of the coating material or the gradual accumulation of wear debris on the surface. In contrast, the S2 coating showed a markedly different friction behavior. The friction coefficient of the S2 coating only increased to 0.42 for the same sliding time and remained stable throughout the process. These results suggest that the S2 coating is capable of providing more stable frictional performance over longer periods of time. This improved stability was primarily attributed to the significant increase in the WC content and the precipitation of larger carbides on the surface of the S2 coating. These carbides, known for their high hardness and abrasion resistance, significantly enhanced the wear resistance of the coating by forming extensive regions, thereby reducing plastic deformation and wear depth, minimizing fluctuations in the friction coefficient, and ensuring stability under dynamic friction conditions [53].

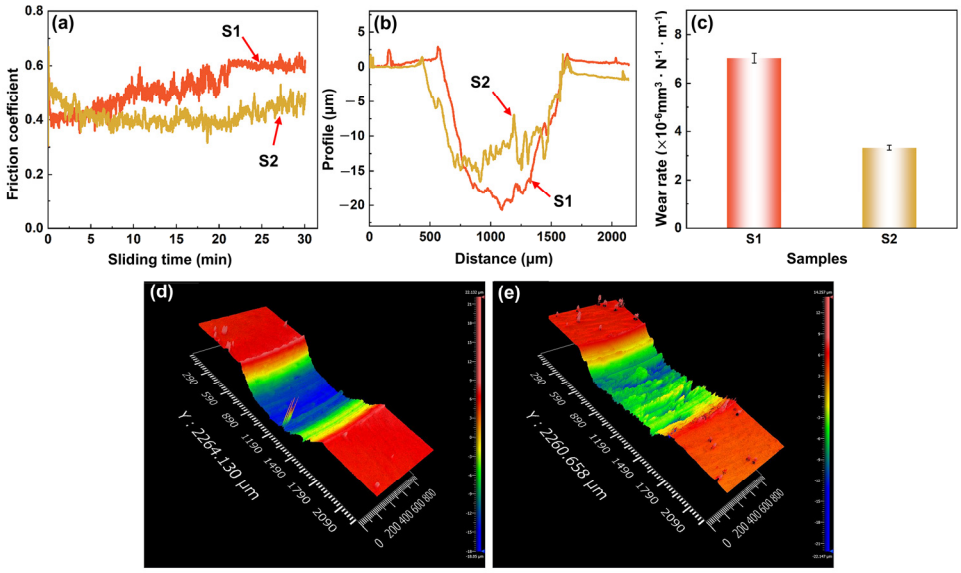


Figure 7. Wear data of S1 and S2 coatings: (**a**) friction coefficient; (**b**) wear profile; (**c**) wear rate; (**d**) 3D morphology of the S1 coating; and (**e**) 3D morphology of the S2 coating.

In Figure 7c, the wear rate measurements show that the S2 coating outperformed, with an impressive wear rate of 3.329×10^{-6} mm^3 (N·m)$^{-1}$, which was 3.709×10^{-6} mm^3 (N·m)$^{-1}$ lower than that of the S1 coating. This significant difference underscores the superior wear resistance of the S2 coating, which effectively minimized the material volume loss during friction. In addition, as shown in Figure 7b, the wear depth of the S2 coating was significantly shallower, further confirming its improved durability and stability under prolonged sliding friction conditions.

Figure 7d,e show the 3D morphologies of the S1 and S2 coatings, visualizing the wear characteristics of both coatings. The surface of the S1 coating shows a larger area of blue color, indicating a greater depth of wear, suggesting that the surface material of the S1 coating was significantly removed during long-term friction. In contrast, the surface of the S2 coating shows a predominantly green color and an uneven distribution, consistent with the distribution of carbides in the coating. As wear progresses, hard particles in the coating may detach or flake from the surface, forming bumps or pits. However, the overall wear of the S2 coating was flatter and more uniform, giving it better durability and stability.

3.5.2. Wear Morphological Analysis

The analysis of the wear morphology further elucidated the wear mechanisms of the S1 and S2 coatings. As depicted in Figure 8a–d, the wear width of the S1 coating was significantly greater, approximately 16 μm wider than that of the S2 coating. Additionally, the S1 coating exhibited pronounced deep groove structures on its surface. The EDS analysis in Figure 8(b1) reveals the presence of significant amounts of nickel, oxygen, and iron on the worn surface. The S1 coating also showed clear signs of surface degradation, such as spalling and distinct regions of nickel accumulation. Figure 8(b1) clearly demonstrates that wear led to the substantial migration of iron from the GCr15 ball to the coating surface, contributing to its degradation. In contrast, the worn surface of the S2 coating displayed the presence of WC particles and hard particles, alongside evidence of adhesive wear. The spectral analysis in Figure 8(d1) shows only trace amounts of Ni, O, and Fe elements on the surface. The incorporation of WC particles significantly enhanced the durability of the nickel-based coating. The primary wear mechanisms for the S1 coating included adhesive wear, abrasive wear, and oxidative wear, whereas the S2 coating predominantly exhibited adhesive wear with minor oxidative wear [54].

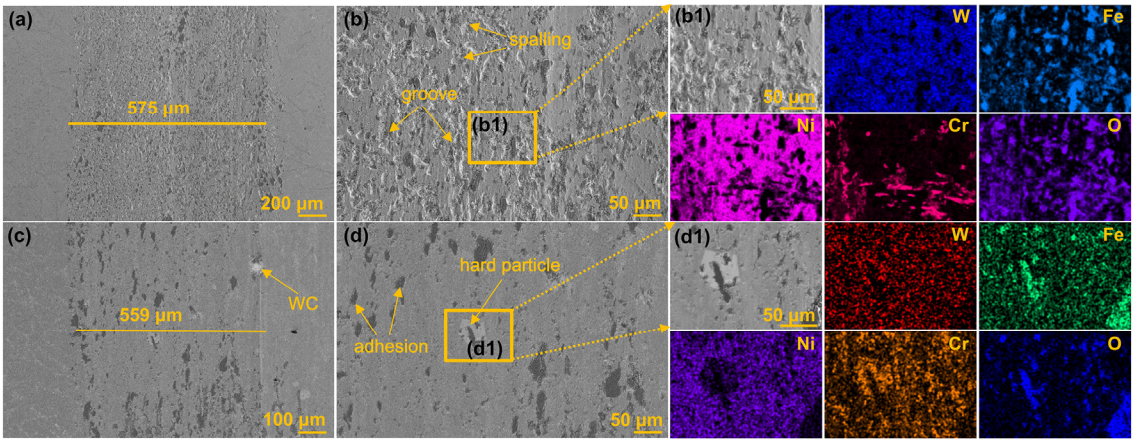


Figure 8. Wear morphologies of the coatings: (**a**–**b1**) S1; (**c**–**d1**) S2.

3.6. Mechanical Properties of the Coatings

3.6.1. Tensile Curve Analysis

According to the results in Figure 9, the stresses and strains gradually decreased as the WC content increased, indicating a significant negative correlation between the WC content and the internal stresses and strains in plasma-arc surfacing. This was attributed to the higher concentration of WC particles in the base material, which led to a more pronounced aggregation effect. Particle agglomeration occurred as the matrix material decreased, making it difficult to uniformly disperse the cemented carbide particles, a phenomenon also discussed in the literature [55]. As particle agglomeration increased, the effective dispersion of the WC phase became limited, further affecting the mechanical properties of the material.

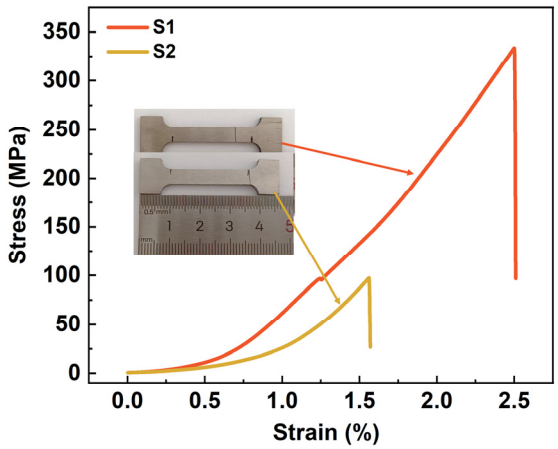


Figure 9. Stress–strain curves of S1 and S2 coatings.

Compared with the S2 coating, the maximum stress and strain of the S1 coating increased significantly to 333 MPa and 2.5%, respectively, indicating that the strength of the S1 coating was increased by 71%, while its ductility was increased by 36%. This strengthening effect was mainly attributed to the complex eutectic arrangement and the remaining transition layer. The eutectic structure typically plays a strengthening role in a multiphase material by hindering dislocation motion, thereby increasing the resistance of the material to deformation under stress–strain conditions [56]. In addition, the remaining transition layer improves the interfacial bonding, thereby increasing the toughness and crack resistance of the material under load. These microstructural features, combined with the distribution of WC particles, work synergistically to improve both the mechanical properties and thermal stability of the material.

3.6.2. Fracture Morphological Analysis

Figure 10 shows significant differences in the fracture morphologies and EDS analysis between the S1 and S2 coatings. The S1 coating exhibited deep dimples, indicating substable plastic deformation prior to fracture, a characteristic of ductile fracture [57]. The deep dimples were mainly composed of γ-(Ni, Fe), as confirmed by EDS analysis (point A in Table 4). The S1 coating was composed of columnar crystals and tungsten carbide particles with an irregular fracture surface showing an inhomogeneous river-like structure, indicating quasi-cleavage characteristics [58]. There were large gaps between the WC particles (Figure 10(a2)).

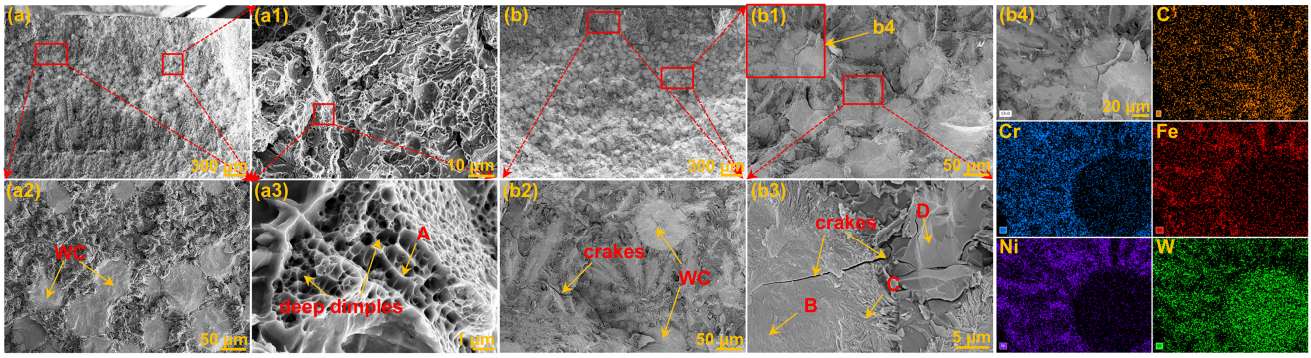


Figure 10. SEM fracture morphologies of the coatings: (**a**–**a3**) S1; (**b**–**b3**) S2; (**b4**) Red box in (**b1**) showing satellite-like structures and chemical composition.

Table 4. Chemical composition of each marker area (at. %).

Area	W	C	Cr	Fe	Ni
A	-	4.23	20.40	22.64	52.73
B	74.70	23.88	0.10	0.24	1.08
C	69.16	25.20	1.16	0.95	3.53
D	53.65	7.36	13.31	4.23	21.45

Conversely, the fracture surface of the S2 coating was smoother, with a higher concentration of WC particles and the absence of a river-like structure (Figure 10b), which was primarily indicative of brittle fracture. In addition, point D in Table 4 shows the formation of cracks propagating along the W_2C phase surrounding the WC and Ni substrates (Figure 10(b3)). The increase in the WC content escalated the crack formation, while the rapid thermal cycling exacerbated the brittleness of the WC particles [59,60]. Figure 10(b4) shows that the edge decomposition products of the WC particles were densely packed and formed a satellite-kind structure composed of Cr, W, and C elements. These elements exhibited high diffusion rates at elevated temperatures, particularly in the high-energy regions at the particle edges [61]. The satellite-kind structure, composed mainly of carbides, easily became a crack initiation point under stress concentration, leading to early fracture. Figure 10(b3) shows that the fracture of the S2 coating was mainly along the hard phase fracture inside the particles or at the edges of the particles [62]. The results show that the fracture mechanism of the S1 coating combined quasi-cleavage fracture and ductile fracture, whereas brittle fracture predominated in the S2 coating. Excessive WC particles reduce the tensile properties of nickel-based coatings.

3.6.3. In Situ Tensile Surface Structure Analysis

In order to better understand the fracture mechanism and crack propagation process, the process of crack initiation and propagation was observed in real time by the combination of an SEM and in situ tensile testing system. Figure 11 is a typical picture of the in-situ stretching process. The surface condition of the S1 coating sample prior to stretching is illustrated in Figure 11a, indicating no presence of internal cracks. Conversely, Figure 11(a1)

showcases the microstructure of the sample after undergoing a stretching duration of 72 s. At this stage, it can be observed that minute cracks started to emerge, with their propagation direction forming an angle close to 90 degrees relative to the axial stretching direction. Cracks mainly appeared in the area where WC aggregates were serious and propagated along WC particles and decomposed hard phases. The findings of this research indicate that there was a higher level of residual stress in the area where WC particles aggregated within the soft nickel-based alloy. When exposed to macroscopic tensile stress, compression occurred among the WC particles, leading to the development of microcracks either inside the coating or near the edges of these particles. Ultimately, fracture occurred due to crack initiation and the combined tensile load, as depicted in Figure 11(a2). The red region in Figure 11(a2) corresponds to Figure 11(a3), as depicted in Figure 11. It becomes apparent that multiple bifurcations occurred near the main crack, with crack propagation primarily initiated from WC particles situated at the outer edge of the main crack. Eventually, the crack extended along the decomposition products of WC particles and ceramic hard phases. As a result of the severe thermal damage experienced by the WC particles, distinct blocky brittle phases precipitated within the coating, leading to decreased toughness and increased susceptibility to cracking. However, no crack initiation was found in the stretching process of the S2 coating, and the entire fracture process took a relatively short time, only 52 s, as shown in Figure 11(b1–b3). The internal binding force was small mainly because the WC particles in the coating were relatively dense. Figure 12 shows the tensile fracture mechanism diagram. Under a constant external load, there was residual stress inside the WC particles, which promoted the formation of micro-cracks at or near the edge of the coating. As the load time increased, these microcracks spread in the WC particles and expanded through the hard phase, eventually causing the coating to fracture.

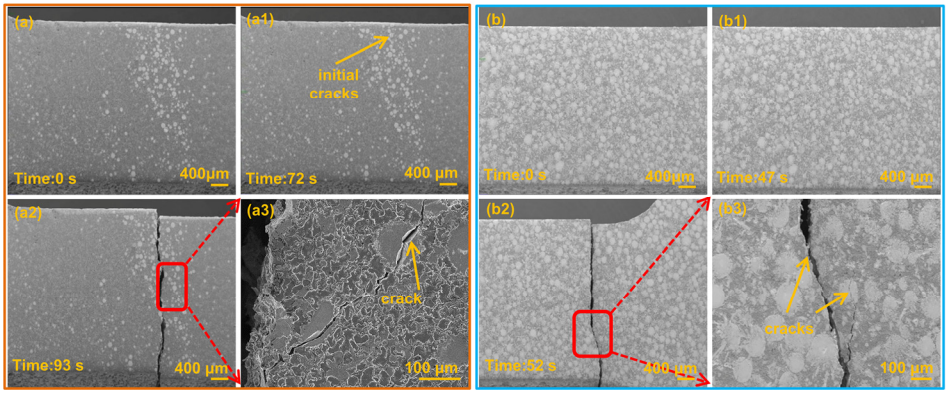


Figure 11. Microstructures of in situ tensile process: (**a**–**a3**) S1; (**b**–**b3**) S2.

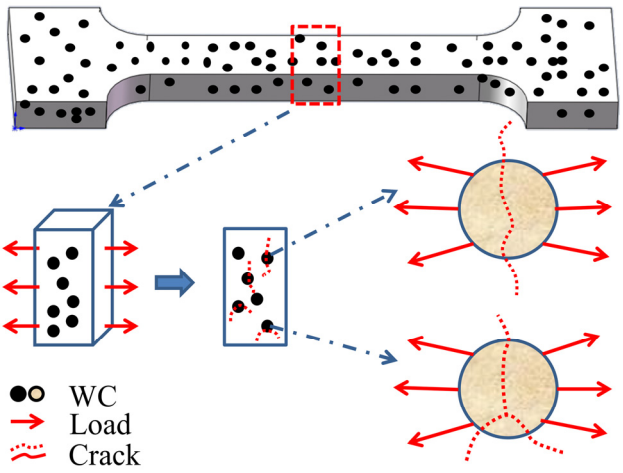


Figure 12. Tensile fracture mechanism diagram.

4. Conclusions

1. With the increase in the WC content from 45% to 65%, the formation of carbides such as M_7C_3, M_6C, and $M_{23}C_6$ increased significantly, while the formation of the γ-phase was inhibited significantly. XPS analysis further revealed that the changes in the WC and Cr_7C_3 phases were particularly prominent in the high-WC content coating, with the binding energies of Fe-C and Cr-C bonds increasing by 0.3 eV and 0.2 eV, respectively. Additionally, the charge transfer between WC and Ni substantially enhanced the bonding strength of the W-C bonds. This finding further confirmed that the stability of the Fe-C, Cr-C, and W-C bonds was significantly improved. These structural changes, together with particle and solid solution strengthening, resulted in an increase in hardness of 232 $HV_{1.0}$ for the 65% WC coating compared with the 45% WC coating.
2. The friction coefficient for the 65% WC coating was remarkably stable and remained low at 0.42, with a wear rate of 3.329×10^{-6} mm^3 $(N{\cdot}m)^{-1}$, a reduction of 3.709×10^{-6} mm^3 $(N{\cdot}m)^{-1}$ compared with the 45% WC coating. The 45% WC coating exhibited a greater wear width (an increase of approximately 16 μm), together with pronounced deep grooves and surface degradation, with the wear mechanisms being predominantly adhesive wear, abrasive wear, and oxidative wear. In contrast, the 65% WC coating exhibited less wear due to the presence of WC particles and hard particles, with the wear mechanism primarily driven by adhesive wear and minor oxidative wear.
3. Conventional tensile tests showed a negative correlation between the WC content and the internal stress and strain of the coatings. Due to the complex eutectic structure and abundant transitional layers, the 45% WC coating exhibited a maximum stress of 333 MPa and strain of 2.5%, which were 71% and 36% higher, respectively, than those of the 65% WC coating. The fracture morphology of the 45% WC coating showed a river-like structure and deep dimples, indicating a fracture mechanism combining ductile and quasi-cleavage properties. In contrast, the fracture of the 65% WC coating was relatively smooth with cracks extending along the W_2C phase, indicating a typical brittle fracture mechanism.
4. In situ tensile tests coupled with SEM observations revealed that in the 65% WC coating, the WC particles were denser, with weaker internal bonding, leading to a shorter fracture process of only 52 s. Conversely, the fracture time for the 45% WC coating extended to 72 s, with cracks originating in the WC aggregation area and propagating along the WC particles and decomposed hard phases.

Author Contributions: L.Z., conceptualization, methodology, validation, data curation, and writing—original draft preparation; S.L., conceptualization, project administration, and funding acquisition; C.Z., methodology and validation; S.Z., investigation and data curation; X.A., conceptualization and supervision; Z.X., methodology, writing—review and editing, and project administration. All authors have read and agreed to the published version of the manuscript.

Funding: This work was supported by the National Key Research and Development Program (no. 2021YFB3702004) of the Ministry of Science and Technology of the People's Republic of China.

Data Availability Statement: The data presented in this study are available upon request from the corresponding author due to privacy.

Conflicts of Interest: The authors declare no conflicts of interest.

References

1. Ramezani, M.; Mohd Ripin, Z.; Pasang, T.; Jiang, C.P. Surface engineering of metals: Techniques, characterizations and applications. *Metals* **2023**, *13*, 1299. [CrossRef]
2. Tian, J.Y.; Hu, Y.; Zhao, H.W.; Hu, Y.; Li, Y.; Zhou, S.L.; Cao, C.Y.; Zhang, L. The indentation and wear performance of hardfacing layers on H13 steel for use in high temperature application. *AIP Adv.* **2019**, *9*, 095304. [CrossRef]

3. Sun, D.S.; Yang, Y.; Liu, Z.; Han, J.Y.; Ma, S.T.; Xu, B.; Yuan, M.Y. Study of design and microstructure properties of laser clad multiphase coupled nickel-based self-lubricating coatings. *J. Mater. Eng. Perform.* **2024**, *33*, 6314–6330. [CrossRef]
4. Lisiecki, A.; Ślizak, D. Hybrid laser deposition of composite WC-Ni layers with forced local cryogenic cooling. *Materials* **2021**, *14*, 4312. [CrossRef]
5. Li, J.F.; Zhu, Z.C.; Peng, Y.X.; Shen, G. Phase evolution and wear resistance of in-situ synthesized $(Cr, W)_{23}C_6$-WC composite ceramics reinforced Fe-based composite coatings produced by laser cladding. *Vacuum* **2021**, *190*, 110242. [CrossRef]
6. Zhang, K.; Ju, H.C.; Xing, F.; Wang, W.; Li, Q.; Yu, X.F.; Liu, W.J. Microstructure and properties of composite coatings by laser cladding Inconel 625 and reinforced WC particles on non-magnetic steel. *Opt. Laser Technol.* **2023**, *163*, 109321. [CrossRef]
7. Hu, Y.J.; Wang, Z.X.; Pang, M. Effect of WC content on laser cladding Ni-based coating on the surface of stainless steel. *Mater. Today Commun.* **2022**, *31*, 103357. [CrossRef]
8. Zhou, S.F.; Zeng, X.Y.; Hu, Q.W.; Huang, Y.J. Analysis of crack behavior for Ni-based WC composite coatings by laser cladding and crack-free realization. *Appl. Surf. Sci.* **2008**, *255*, 1646–1653. [CrossRef]
9. Liu, S.L.; Zheng, X.P. Microstructure and properties of AC-HVAF sprayed Ni60/WC composite coating. *J. Alloy Compd.* **2009**, *480*, 254–258. [CrossRef]
10. Ma, Q.S.; Li, Y.J.; Wang, J.; Liu, K. Investigation on cored-eutectic structure in Ni60/WC composite coatings fabricated by wide-band laser cladding. *J. Alloy Compd.* **2015**, *645*, 151–157. [CrossRef]
11. Boonyongmaneerat, Y.; Saengkiettiyut, K.; Saenapitak, S.; Sangsuk, S. Effects of WC addition on structure and hardness of electrodeposited Ni–W. *Surf. Coat. Technol.* **2009**, *203*, 3590–3594. [CrossRef]
12. Bartkowski, D.; Młynarczak, A.; Piasecki, A.; Dudziak, B.; Gościański, M.; Bartkowska, A. Microstructure, microhardness and corrosion resistance of Stellite-6 coatings reinforced with WC particles using laser cladding. *Opt. Laser Technol.* **2015**, *68*, 191–201. [CrossRef]
13. Li, W.Y.; Yang, X.F.; Xiao, J.P.; Hou, Q.M. Effect of WC mass fraction on the microstructure and friction properties of WC/Ni60 laser cladding layer of brake discs. *Ceram. Int.* **2021**, *47*, 28754–28763. [CrossRef]
14. Li, X.N.; Zhang, S.Y.; Liu, W.; Pang, X.T.; Tong, Y.G.; Zhang, M.J.; Zhang, J.; Wang, K.M. Effect of WC content on the wear and corrosion properties of oscillating laser-cladding-produced nickel-based coating. *Coatings* **2023**, *13*, 1614. [CrossRef]
15. Wang, H.T.; Chen, X.; Bai, X.B.; Ji, G.C.; Dong, Z.X.; Yi, D.L. Microstructure and properties of cold sprayed multimodal WC–17Co deposits. *Int. J. Refract. Met. H.* **2014**, *45*, 196–203. [CrossRef]
16. Huang, J.H.; He, J.C.; Li, Z.J.; Shen, L.; Chen, L.; Chang, F.; Dai, P.Q.; Tang, Q.H. Effect of WC addition on microstructure and properties of powder metallurgy CoCrNi medium entropy alloy. *Mater. Today Commun.* **2023**, *36*, 106435. [CrossRef]
17. Yue, K.; Wang, L.; Xu, Z.; Cheng, C.L.; Wang, Y.Q.; Fan, Y.; Xu, J.; Wang, Z.J.; Chen, Z. Effect of WC content on the microstructure and wear resistance of laser cladding AlCoCrFeNiTi0.5 high-entropy alloy coatings. *Ceram. Int.* **2024**, S0272884224034163. [CrossRef]
18. Luo, K.X.; He, J.Y.; Ma, H.; Wang, C.; Lu, J.; Li, C.; Peng, Y.D.; Wu, N.; Luo, F.H. Dissolution behaviour of WC particles and evolution of precipitated phases in the plasma transfer arc Ni-based composite coating reinforced by 30 wt.% WC particles. *Ceram. Int.* **2024**, *50*, 35065–35078. [CrossRef]
19. Kleykamp, H. Thermodynamic studies on chromium carbides by the electromotive force (Emf) method. *J. Alloy Compd.* **2001**, *321*, 138–145. [CrossRef]
20. Wu, P.; Du, H.M.; Chen, X.L.; Li, Z.Q.; Bai, H.L.; Jiang, E.Y. Influence of WC particle behavior on the wear resistance properties of Ni–WC composite coatings. *Wear* **2004**, *257*, 142–147. [CrossRef]
21. Guo, C.; Chen, J.M.; Zhou, J.S.; Zhao, J.R.; Wang, L.Q.; Yu, Y.J.; Zhou, H.D. Effects of WC-Ni content on microstructure and wear resistance of laser cladding Ni-based alloys coating. *Surf. Coat. Technol.* **2012**, *206*, 2064–2071. [CrossRef]
22. Zhang, Y.M.; Hida, M.; Sakakibara, A.; Takemoto, Y. Effect of WC addition on microstructures of laser melted Ni-based alloy powder. *Surf. Coat. Technol.* **2003**, *169–170*, 384–387. [CrossRef]
23. Shen, X.H.; He, X.P.; Gao, L.Y.; Su, G.S.; Xu, C.H.; Xu, N. Study on crack behavior of laser cladding ceramic-metal composite coating with high content of WC. *Ceram. Int.* **2022**, *48*, 17460–17470. [CrossRef]
24. Tan, N.; Hu, Z.Y.; Zhou, Y.J.; Li, Y.; Lu, B.W.; Hu, D.C.; Liu, Y.; Li, Q. Effect of WC particle size on the microstructure and tribological properties of high-speed laser cladding Ni/WC composite coatings. *Mater. Today Commun.* **2024**, *39*, 109066. [CrossRef]
25. He, B. Effect of WC Content on microstructure and properties of WC/316L laser coatings. *Ferroelectrics* **2023**, *608*, 1–12. [CrossRef]
26. Bao, C.G.; Gao, Y.M.; Xing, J.D.; Zhang, G.S. Wear behavior of plasma sprayed Ni-WC composite coatings. *KEM* **2007**, *336–338*, 1731–1733. [CrossRef]
27. Yan, X.C.; Huang, C.J.; Chen, C.Y.; Bolot, R.; Dembinski, L.; Huang, R.Z.; Ma, W.Y.; Liao, H.L.; Liu, M. Additive manufacturing of WC reinforced maraging steel 300 composites by cold spraying and selective laser melting. *Surf. Coat. Technol.* **2019**, *371*, 161–171. [CrossRef]
28. Bello, Z.A.; Kang, M.; Ndumia, J.N.; Geng, C.; Jibril, A.N.; Liu, J. Microstructure and properties of WC-reinforced AlCoCrFeNiSi high entropy alloy coatings prepared via high-velocity arc spraying. *Mater. Today Commun.* **2024**, *40*, 109705. [CrossRef]
29. Zhang, M.Y.; Li, M.; Chi, J.; Wang, S.F.; Yang, S.; Yang, J.; Wei, Y.J. Effect of Ti on microstructure characteristics, carbide precipitation mechanism and tribological behavior of different WC types reinforced Ni-based gradient coating. *Surf. Coat. Technol.* **2019**, *374*, 645–655. [CrossRef]

30. Baturin, A.; Lotkov, A.; Grishkov, V.; Rodionov, I.; Kudiiarov, V. Effect of hydrogen redistribution during aging on the structure and phase state of nanocrystalline and coarse-grained TiNi alloys. *J. Alloy Compd.* **2018**, *751*, 359–363. [CrossRef]
31. Petrushin, N.; Hvatzkiy, K.; Link, T.; Epishin, A.; Nolze, G.; Gerstein, G. A single-crystal Co-base superalloy strengthened by γ' precipitates: Structure and mechanical properties. *Adv. Eng. Mater.* **2015**, *17*, 755–760. [CrossRef]
32. Zhou, S.F.; Dai, X.Q. Laser induction hybrid rapid cladding of WC particles reinforced NiCrBSi composite coatings. *Appl. Surf. Sci.* **2010**, *256*, 4708–4714. [CrossRef]
33. Liu, F.F.; Liaw, P.K.; Zhang, Y. Recent progress with BCC-structured high-entropy alloys. *Metals* **2022**, *12*, 501. [CrossRef]
34. Zhang, J.; Li, J.; Shi, C.B.; Li, J.H. Evolution of eutectic carbide during M_7C_3 /$M_{23}C_6$ in situ transformation in martensitic stainless steel. *Steel Res. Int.* **2022**, *93*, 2200231. [CrossRef]
35. Ma, Q.; Lu, B.W.; Zhang, Y.M.; Wang, Y.L.; Yan, X.C.; Liu, M.; Zhao, G.R. Crack-free 60 wt.% WC reinforced FeCoNiCr high-entropy alloy composite coating fabricated by laser cladding. *Mater. Lett.* **2022**, *324*, 132667. [CrossRef]
36. Wei, Y.; Wei, X.S.; Chen, B.; Zuo, J.Y.; Ma, T.C.; Shen, J. Parameter optimization for tungsten carbide/Ni-based composite coating deposited by plasma transferred arc hardfacing. *Trans. Nonferrous Met. Soc.* **2018**, *28*, 2511–2519. [CrossRef]
37. Genga, R.M.; Akdogan, G.; Polese, C.; Garrett, J.C.; Cornish, L.A. Abrasion wear, thermal shock and impact resistance of WC-cemented carbides produced by PECS and LPS. *Int. J. Refract. Met. Hard Mater* **2015**, *49*, 133–142. [CrossRef]
38. Kaçmaz, D.; Kalkavan, F.; Yazıcı, S.; Demirural, A.; Baykara, T. Processing, sintering and performance of WC-Co-near-nano TiC metal matrix composites. *RDMS.* **2019**, *9*, 1012–1018. [CrossRef]
39. Detroye, M.; Reniers, F.; Buess-Herman, C.; Vereecken, J. AES–XPS study of chromium carbides and chromium iron carbides. *Appl. Surf. Sci.* **1999**, *144–145*, 78–82. [CrossRef]
40. Li, J.; Liu, C.Y.; Zhao, B.G.; Lin, Y.Q.; Deng, Z.J. Structures and properties of Fe-C particles prepared by AC arc discharge. *J. Magn. Magn. Mater.* **1999**, *195*, 470–475. [CrossRef]
41. Furlan, A.; Jansson, U.; Lu, J.; Hultman, L.; Magnuson, M. Structure and bonding in amorphous iron carbide thin films. *J. Phys. Condens. Matter.* **2015**, *27*, 045002. [CrossRef]
42. Zhang, Y.; Chen, Y.; Zhao, Y.W.; Xiang, N. Photocatalytic activity and microstructure of micro-Arc oxidized TiO2: Cr^{3+} com-posite coatings. *Mater. Technol.* **2018**, *33*, 592–602. [CrossRef]
43. Lynch, B.; Wang, Z.; Ma, L.; Paschalidou, E.M.; Wiame, F.; Maurice, V.; Marcus, P. Passivation-induced Cr and Mo enrichments of 316L stainless steel surfaces and effects of controlled pre-oxidation. *J. Electrochem. Soc.* **2020**, *167*, 141509. [CrossRef]
44. Håkansson, K.L.; Johansson, H.I.P.; Johansson, L.I. High-resolution core-level study of hexagonal WC (0001). *Phys. Rev. B* **1994**, *49*, 2035–2039. [CrossRef]
45. Sivkov, D.; Nekipelov, S.; Petrova, O.; Vinogradov, A.; Mingaleva, A.; Isaenko, S.; Makarov, P.; Ob'edkov, A.; Kaverin, B.; Gusev, S.; et al. Studies of buried layers and interfaces of tungsten carbide coatings on the MWCNT surface by XPS and NEXAFS spec-troscopy. *Appl. Sci.* **2020**, *10*, 4736. [CrossRef]
46. Song, D.; Shin, J.; Lee, Y.; Kwon, Y.; Lim, J.; Kim, E.-J.; Oh, S.; Kim, M.; Cho, E. Thin nickel layer with embedded WC nano-particles for efficient oxygen evolution. *ACS Appl. Energy Mater.* **2019**, *2*, 3452–3460. [CrossRef]
47. Li, Y.L.; Song, P.; Wang, W.Q.; Lei, M.; Li, X.W. Microstructure and wear resistance of a Ni-WC composite coating on titanium grade 2 obtained by electroplating and electron beam remelting. *Mater. Charact.* **2020**, *170*, 110674. [CrossRef]
48. Wu, H.Y.; Dong, Y.P.; Li, X.W.; Li, Y.L.; Yan, M. First principle calculations and low cost SLM processing of Ti-TiB composite materials. *Mater. Sci. Eng. A* **2021**, *803*, 140711. [CrossRef]
49. Li, Y.L.; Wu, Y.Y.; Wang, W.Q.; Lei, M.; Li, X.W. Microstructure and mechanical properties of the Ni-B-Ti composite coating on TA2 prepared by pre-plating and laser remelting. *Surf. Coat. Technol.* **2021**, *405*, 126567. [CrossRef]
50. Wu, Z.L.; Wang, W.Q.; Li, X.W.; Yan, M.; Li, Y.L. Microstructure and mechanical properties of Ti-6Al-4V prepared by nickel preplating and electron beam surface remelting. *J. Mater. Process. Technol.* **2019**, *271*, 420–428. [CrossRef]
51. Ren, S.; Li, J.; Fang, Q.; Feng, H. Effect of solid solution addition on the dislocation emission in aluminum alloys. *Acta Mech.* **2020**, *231*, 4537–4545. [CrossRef]
52. Melendez, N.M.; McDonald, A.G. Development of WC-Based metal matrix composite coatings using low-pressure cold gas dynamic spraying. *Surf. Coat. Technol.* **2013**, *214*, 101–109. [CrossRef]
53. Chen, G.D.; Liu, X.B.; Zhang, F.Z.; Li, M.X.; Zhang, S.H. Refractory ceramic WC reinforced Co matrix composite coatings on IN718 superalloy: Microstructure, wear mechanisms and surface energy. *Tribol. Int.* **2024**, *194*, 109516. [CrossRef]
54. Ma, L.T.; Zhao, D.C.; Wang, Y.H.; Wang, K.B.; Huang, J.; Jin, X.Y.; Kong, D.C.; Wang, M.L.; Yamaguchi, T.; Wang, H.W. Optimized wear behaviors and related wear mechanisms of medium entropy alloy-based composite coatings. *J. Mater. Res. Technol.* **2024**, *29*, 12–27. [CrossRef]
55. Wang, Z.H.; Liu, Y.W.; Liu, K.; Wang, B.X. Mechanical properties and microstructure of spark plasma sintered WC-8 wt.%Co-VC-cBN ultrafine grained cemented carbide. *Ceram. Int.* **2019**, *45*, 23658–23665. [CrossRef]
56. Misra, A.; Hirth, J.P.; Kung, H.; Hoagland, R.G.; Embury, J.D. Dislocation models for strengthening in nanostructured metallic multilayers. *MRS Proc.* **2000**, *634*, B4.2.1. [CrossRef]
57. Yao, Y.Z.; Huang, Y.H.; Chen, B.; Tan, C.W.; Su, Y.; Feng, J.C. Influence of processing parameters and heat treatment on the mechanical properties of 18Ni300 manufactured by laser based directed energy deposition. *Opt. Laser Technol.* **2018**, *105*, 171–179. [CrossRef]

58. Liu, W.; Sha, J.B. Failure mode transition of Nb phase from cleavage to dimple/tear in Nb-16Si-based alloys prepared via spark plasma sintering. *Mater. Des.* **2016**, *111*, 301–311. [CrossRef]
59. Tan, C.; Hu, J.; Shi, Q.; Khanlari, K.; Xie, H.W.; Liu, X. Enhanced hardness and toughness in WC/W2C-Ni-Cu composites fabricated by selective laser melting. *Int. J. Refract. Met. Hard Mater.* **2022**, *105*, 105805. [CrossRef]
60. Domitner, J.; Silvayeh, Z.; Buzolin, R.H.; Krisam, S.; Achterhold, K.; Povoden-Karadeniz, E.; Sommitsch, C.; Mayr, P. Microstructure characterization of nickel matrix composite reinforced with tungsten carbide particles and produced by laser cladding. *Adv. Eng. Mater.* **2022**, *24*, 2200463. [CrossRef]
61. Dong, R.F.; Li, J.S.; Zhang, T.B.; Hu, R.; Kou, H.C. Elements segregation and phase precipitation behavior at grain boundary in a Ni-Cr-W based superalloy. *Mater. Charact.* **2016**, *122*, 189–196. [CrossRef]
62. Qin, J.Y.; Hui, J.Q.; Dong, W.W.; Bai, Y.F.; Fan, J.H.; Ding, H.; Zhu, S.G. Preparation of high-performance WC–MgO composites by spark plasma sintering. *Adv. Eng. Master.* **2022**, *24*, 2200625. [CrossRef]

Disclaimer/Publisher's Note: The statements, opinions and data contained in all publications are solely those of the individual author(s) and contributor(s) and not of MDPI and/or the editor(s). MDPI and/or the editor(s) disclaim responsibility for any injury to people or property resulting from any ideas, methods, instructions or products referred to in the content.